Research Article Vol. 11, No. 9 / September 2024 / Optica 1285

Asynchronous, semi-reverberant elastography

Ginger Schmidt,[1,2,*] Brett E. Bouma,[1,2] and Néstor Uribe-Patarroyo[1]

[1]Wellman Center for Photomedicine, Harvard Medical School and Massachusetts General Hospital, 40 Blossom Street, Boston, Massachusetts 02114, USA
[2]Institute for Medical Engineering and Science, Massachusetts Institute of Technology, Cambridge, 77 Massachusetts Avenue, Massachusetts 02139, USA
*gingers@mit.edu

Received 1 May 2024; revised 10 August 2024; accepted 12 August 2024; published 10 September 2024

Optical coherence elastography measures elasticity—a property correlated with pathologies such as tumors due to fibrosis, atherosclerosis due to heterogeneous plaque composition, and ocular diseases such as keratoconus and glaucoma. Wave-based elastography, including reverberant elastography, leverages the properties of shear waves traveling through tissue primarily to infer shear modulus. These methods have already seen significant development over the past decade. However, existing implementations in OCT require robust synchronization of shear wave excitation with imaging, complicating widespread clinical adoption. We present a method for complete recovery of the harmonic shear wave field in an asynchronous, conventional frame-rate, raster-scanning OCT system by modeling raster-scanning as an amplitude modulation of the displacement field. This technique recovers the entire spatially and temporally coherent complex-valued shear wave field from just two B-scans, while reducing the time scale for sensitivity to motion from minutes to tens of milliseconds. To the best of our knowledge, this work represents the first successful demonstration of reverberant elastography on a human subject *in vivo* with a conventional frame-rate, raster-scanning OCT system, greatly expanding opportunity for widespread translation.

https://doi.org/10.1364/OPTICA.528507

1. INTRODUCTION

Optical coherence tomography (OCT) has enabled high resolution imaging of subsurface micro-structure in biological tissues. By leveraging interferometry to measure light reflected from a sample, OCT can acquire depth-resolved cross-sectional images with a lateral resolution of a few microns and penetration depth of a few millimeters [1]. OCT has seen the most clinical adoption in ophthalmology; however, its compatibility with fiber optics also makes it well suited for imaging internal organs through catheters or endoscopes [2–4]. Despite its utility, existing OCT systems lack the ability to robustly and conveniently measure tissue properties such as stiffness and compliance—properties highly correlated with ocular pathologies such as keratoconus, intraocular pressure dysregulation, and glaucoma [5–8]. Beyond ophthalmology, there are many other pathologies that modulate elasticity, such as tumors due to fibrosis [9], pulmonary fibrosis due to thickening of alveolar walls [10], and atherosclerosis due to heterogeneous plaque composition and calcification [11,12]. To image stiffness, optical coherence elastography (OCE) is a functional extension of OCT that tracks internal displacements due to external forces [13]. These forces range from quasi-static compression [14], to passive excitation from natural bodily motions such as the heartbeat [15,16], to dynamically actuated shear waves [17–21]. The measured displacements that occur as a result of external forces are correlated with a mechanical model, and parameters such as shear modulus can be derived.

Wave-based OCE methods leverage the properties of shear waves traveling through tissue primarily to infer shear modulus. Compared to compression methods, wave-based methods do not require sensitive reference measurements or computationally intense finite-element modeling. Passive shear wave excitation is appealing due to its simplicity; however, natural bodily motions are limited in frequency content and may be too uncontrollable depending on the clinical target. Dynamic OCE is a promising wave-based method that uses a unidirectional wavefront to measure shear wave speed [21,22]. Another promising wave-based method is reverberant elastography, which uses multiple points of excitation to generate a harmonic and diffuse shear wave field [23]. The reverberant field is in essence a near-field shear wave speckle field produced by the coherent superposition of fully randomized shear waves [24,25]. It represents an underlying relationship between shear wave speckle size and shear wavelength, so correlations of the field enable measurements of localized shear wave number. Compared to unidirectional wavefront methods, reverberant OCE could be more robust against motion artifacts and complex tissue structures due its ability to leverage multiple wavefronts and wave reflections at boundaries. It is also a 3D volumetric technique, rather than a 1D technique (although it still requires significant averaging along at least two dimensions, on the scale of the shear wavelength). In this work, we will focus on enabling reverberant elastography, although the shear wave

recovery techniques we present may also be applicable to other wave-based methods.

Despite reverberant elastography's promising theoretical benefits, there remain practical limitations regarding its implementation. Most limiting is the relatively slow speed of OCT raster-scanning (for conventional wavelength-sweep rates <100 kHz) compared to rapidly propagating shear waves. To overcome this, state-of-the-art methods require reproducible synchronization (or pseudo-synchronization) of shear wave excitation with imaging to acquire MB-mode scans. MB-mode scans are B-scans composed of M-mode scans acquired consecutively at each lateral position. In the cornea, reverberant elastography has been demonstrated with a 100 × 100 lateral sampling volume necessitating an acquisition time of 1 min [26]. The nature of MB-mode scanning implies that any motion during the volumetric acquisition will destroy the coherence of the diffuse shear wave field and hamper analysis. This limitation may explain the lack of widespread clinical translation of reverberant elastography in humans *in vivo*, despite promising results in tissue *ex vivo*, mice *in vivo* with a cranial window [27], and zebrafish embryo on a petri dish [28]. Notably, faster A-line rates in general do not enable shorter acquisition times either. Synchronization relies on observing a whole number of periods of the wave field, which is a function of wave frequency, not A-line rate. Line-field holography [29] and MHz OCT systems [30] have both been proposed to address this practical limitation with some success. Despite their promise, these solutions rely on complex, custom hardware, which may limit their clinical translation. Altogether, reverberant elastography still has potential for elasticity imaging *in vivo*. Its primary limitation (and the limitation of many other wave-based OCE methods) is of a practical matter: complexity of imaging rapidly moving shear waves.

In this work, we demonstrate complete recovery of a harmonic reverberant shear wave field in a raster-scanning configuration without the need for synchronization. This is achieved by modeling raster-scanning as an amplitude modulation of the displacement field. We also present the first demonstration of asynchronous semi-reverberant elastography in a layered phantom and in human skin *in vivo* before and after hydration, opening the door for elasticity contrast in conventional OCT systems. Our experimental results *in vivo* demonstrate the feasibility of our technique for diagnosing and/or monitoring pathologies in patients correlated with skin elasticity, such as skin cancer lesions and systemic sclerosis [31–33]. Pivotal to enabling reverberant elastography *in vivo* and in conventional OCT systems is the fact that our technique *reduces the time scale for sensitivity to motion artifacts from minutes to tens of milliseconds*. This work enables OCT elasticity measurements with the same acquisition time required for OCT angiography, greatly expanding the opportunity for widespread application of OCE *in vivo*. To the best of our knowledge, this work represents the first successful demonstration of reverberant elastography with a conventional frame-rate, raster-scanning OCT system without the need for synchronization or complex, custom hardware.

2. METHODS

A. Asynchronous Semi-reverberant Elastography Theory

1. Overcoming Temporal Coherence Limitations

Hereafter, we denote vectors in bold type $\mathbf{v}$ and unitary vectors as $\hat{\mathbf{v}}$. The right-handed coordinate system is defined such that the optical axis or depth direction is z (increasing in depth), in-plane lateral dimension is x, and out-of-plane lateral dimension is y. Phase-sensitive Doppler OCT measures shear wave displacements, so we are only sensitive to displacements along the z-axis [34]. Reverberant shear waves are modeled as the superposition of plane waves propagating in many random directions. The particle displacement $\mathbf{S}(\boldsymbol{\varepsilon}, t)$ of the shear wave field as a function of position $\boldsymbol{\varepsilon} = \{\varepsilon_x, \varepsilon_y, \varepsilon_z\}$ and time t is defined by

$$\mathbf{S}(\boldsymbol{\varepsilon}, t) = \sum_{q,l} \hat{\mathbf{n}}_{ql} s_{ql} e^{j(k\hat{\mathbf{n}}_q \cdot \boldsymbol{\varepsilon} - \omega_0 t)}, \tag{1}$$

where the propagation direction of each wave is $\hat{\mathbf{n}}_q$ and is defined in the spherical coordinate system by angles ϕ and θ [see Fig. 1(a)]. The imaginary constant is j. The polarization $\hat{\mathbf{n}}_{ql}$ of each wave is normal to the direction of propagation, so it is defined as lying on the plane orthogonal to $\hat{\mathbf{n}}_q$ with its orientation given by a third angle, α. The amplitude and phase of each wave are denoted by s_{ql}, k is the shear wave number, and ω_0 is the shear wave frequency.

This derivation follows closely the previous work by Parker *et al.* [23] with a crucial difference: in their work, the shear wave field

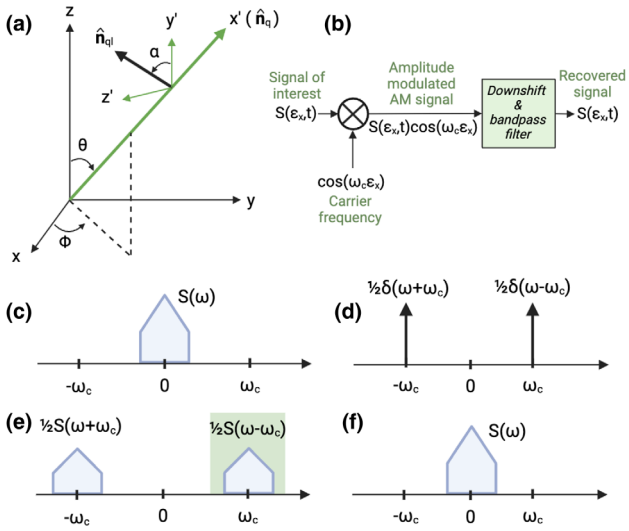

Fig. 1. Shear wave propagation direction and polarization are defined by $\hat{\mathbf{n}}_q$ and $\hat{\mathbf{n}}_{ql}$, respectively (a). If there is a time delay between A-lines from the same B-scan (such as from raster-scanning), the signal of interest $\mathbf{S}(\boldsymbol{\varepsilon}, t)$ is modulated by a carrier frequency related to the shear wave frequency and scanning speed (b). Recovery of the desired signal is illustrated in the frequency domain. To observe the effect of amplitude modulation and understand how to demodulate it, first compute the Fourier transform of the displacement field (c). Then, the amplitude modulation cosine term is equivalent to two impulses at the positive and negative carrier frequencies (d). Since amplitude modulation is a multiplication in the spatial domain, we compute the convolution between the cosine term and the displacement field in the frequency domain. This results in two copies of the signal, each scaled by half (e). From this representation, it is straightforward to recover the original signal. Apply a bandpass filter around the carrier frequency as represented by the green box (e), then downshift it (f) and compute the inverse Fourier transform.

was represented by the particle *velocity* rather than the *displacement*. This distinction is notable because the relatively fast speed of shear waves (1–10 m/s) compared to conventional, raster-scanned OCT frame rates (<1 kHz) makes it infeasible to directly measure particle velocity from frame to frame. As a result, prior work synchronized shear wave excitation with MB-mode scanning to acquire multiple A-lines in the same location without scanning. The data were then stitched together to produce a fully coherent shear wave velocity field. While this effectively increased frame rates to be essentially equal to the laser sweep repetition rate, it led to many practical limitations such as increased acquisition time and higher sensitivity to motion. We propose leveraging the displacement rather than the velocity because displacement measurements relative to an initial frame do not require such fast frame rates. Furthermore, shear waves are modeled as complex exponential plane waves, so the displacement and velocity fields are mathematically identical beyond a scaling factor and $\pi/2$ phase shift.

Given the definition of the shear wave field in Eq. (1), the normalized ensemble average of the autocorrelation of the displacement yields an analytical expression that is a function of shear wave number k. In other words, the expected value of the shear wave speckle size depends only on shear wavelength for a fully randomized superposition of waves. The autocorrelation is computed individually at each time step only with respect to $\boldsymbol{\varepsilon}$, so $\Delta t = 0$. We focus here on the spatial correlation with respect to the fast raster-scanning axis x along which B-scans are acquired, but a similar process may be followed along the other dimensions, yielding a slightly different result along the z-axis (like in Eq. 3 in Zvietcovich *et al*. [26]). This results in a sum of spherical Bessel functions:

$$B_{S_z S_z}(\Delta\varepsilon_x, \Delta t) = j_0(k\Delta\varepsilon_x) - \frac{j_1(k\Delta\varepsilon_x)}{k\Delta\varepsilon_x}, \tag{2}$$

where S_z is the displacement along the sensor axis, ε_x is the B-scan axis along which the beam is scanned, and Δ represents the difference along a given dimension for which the autocorrelation is calculated. While the normalized autocorrelations for the displacement and velocity fields are identical, one crucial benefit is that displacement measurements avoid the requirement for temporal coherence, thereby drastically reducing frame rate requirements and removing one of the needs for MB-mode scanning and shear wave synchronization.

2. Accounting for Raster-Scanning

We have reduced temporal sampling requirements by leveraging the displacement rather than velocity. However, raster-scanning also introduces a time delay between individual A-lines from within a single B-scan. At a glance, this time delay distorts shear wave measurements by introducing a high frequency term [see Fig. 4(b)], making straightforward, conventional measurements of the autocorrelation infeasible. To adapt the autocorrelation for asynchronous raster-scanning, t is no longer constant within a B-scan. For the i-th OCT frame, time is represented by $t_i + \Delta x/v_{\text{scan}}$, where $\Delta x = x - x_0$ is the distance away from the initial A-line x_0, and v_{scan} is the in-plane raster-scanning speed. If we set $x_0 = 0$, the displacement becomes

$$\mathbf{S}(x, t_i) = \sum_{q,l} \hat{\mathbf{n}}_{ql} s_{ql} e^{j[k\hat{\mathbf{n}}_q \cdot \boldsymbol{\varepsilon} - \omega_0 (t_i + x/v_{\text{scan}})]}. \tag{3}$$

The real component of this displacement field compared to previous implementations reveals a key difference between synchronous and asynchronous imaging: the term $\cos(\omega_0 x/v_{\text{scan}})$. This term may be interpreted as a modulation by the carrier frequency ω_0/v_{scan} [see Fig. 1(b)]. When viewed in the frequency domain, we can conveniently recover the spatially coherent displacement field. As illustrated in Figs. 1(c)–1(f), the signal of interest is shifted to both the positive and negative carrier frequency in the Fourier domain when amplitude is modulated by raster-scanning. To recover the analytical signal of interest, compute the Fourier transform of the modulated signal, downshift the spectrum by the carrier frequency such that one copy of the desired signal is centered at zero, apply a bandpass filter to suppress the second mirrored copy, and compute the inverse Fourier transform. The resulting (now spatially coherent) displacement field is complex. The real component gives the displacement field at one point in time, but we can also leverage the phase to produce the entire harmonic shear wave field [see Visualization 1].

This reveals yet another crucial discovery: the analytical representation of the displacement field contains all the information needed to generate the entire wave field at any point in time. Simply multiply the complex field by a corresponding exponential phase term to produce the shear wave field at a different point in time. Furthermore, *we only need two OCT B-scans at each location to measure all possible information about the shear wave field*. See Visualization 1 for a demonstration of an entire shear wave period generated from just *two* raster-scanned B-scans. This is a major improvement over previous shear wave imaging methods, which hold their beams at the same physical single location until at least one entire period of the shear wave field has passed. Since MB-mode scanning speeds are dictated by shear wave excitation frequency (often around 2 kHz) and not laser sweep repetition rates, even a faster laser will not increase the acquisition speed of previous methods. Indeed, increasing the laser sweep rate would simply result in the acquisition of redundant data. In comparison, raster-scanning allows us to recover a concise and sufficient data set from just *two* asynchronous B-scans, thus yielding a near 100-fold increase in acquisition speed.

3. In-Plane Plow Excitation

Demodulation allows us to recover the displacement field along the x-dimension, which is the fast B-scanning axis. However, scanning in the out-of-plane y-dimension is too slow, and the asynchronous behavior makes the phase of the shear wave field too unreliable to recover spatial coherence between separate neighboring B-scans along y. This is the last practical limitation we overcame to achieve asynchronous raster-scanned reverberant elastography. In previous reverberant elastography implementations, a 2D-autocorrelation was calculated along the *entire* xy-plane and averaged azimuthally to obtain one 1D radial autocorrelation function for each 2D window [26]. This procedure was required because the shear wave speckle field has a well-defined local direction of propagation that changes randomly and continuously in space at the length scale of shear wave speckle. However, with asynchronous imaging, we can only recover the shear wave field along the B-scanning x-axis. Therefore, the autocorrelation can only be validly computed along the B-scanning x-axis. Furthermore, identically sized waves traveling at different angles relative to the B-scan plane will appear to have different wavelengths [see Fig. 2(c)]. To address this limitation, we propose a novel semi-reverberant excitation scheme that

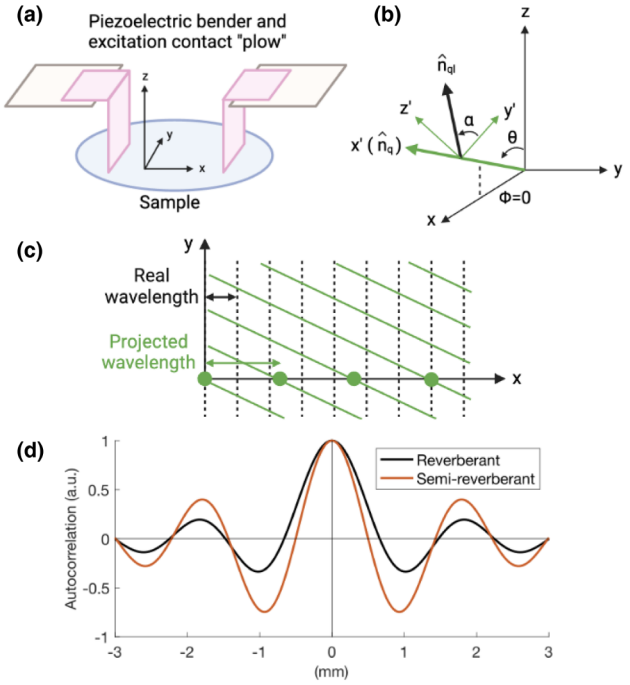

Fig. 2. In-plane semi-reverberant shear waves are generated by 3D-printed prongs called "plows" (a). Since shear waves only propagate within the xz-plane, let $\phi = 0$ when computing the ensemble average (b). When $\phi \neq 0$, such as the wave represented by solid green lines in (c), the shear wavelength projected onto the x-axis will be larger than expected. It is impossible to detangle out-of-plane waves without coherent measurements along the y-axis, which we do not have. Instead, we limit waves to only traveling in-plane with B-scans. The resulting Bessel function sum is similar to the fully reverberant case, but narrower (d).

only generates waves traveling in-plane with B-scans to completely avoid out-of-plane waves. This is achieved by a new approach that may be termed "plow excitation," as shown in Fig. 2(a).

In-plane waves are shear waves for which the direction of propagation $\hat{\mathbf{n}}_q$ is parallel to the B-scan xz-plane [Fig. 2(b)]. Equivalently, $\phi = 0$. This approximation may seem limiting; however, current strategies for generating reverberant shear wave fields and evaluations of the reverberant extent of a field remain ambiguous. Therefore, this narrower definition of the shear wave field could ease ambiguity surrounding the reverberant nature of a wave field, while also simplifying wave excitation strategies. For example, in work such as that by Flores *et al*. [35], 60 incident plane waves were necessary to create a reverberant field, while in other work such as that by Kabir *et al*. [36], only one mechanical driver was required for constrained organs such as the brain. These studies exemplify how variable tissue types can impact the quality and excitation strategy for a fully reverberant wave field, and there are not consistent metrics for validating reverberant fields beyond simulation and experimental testing. If waves are limited to the B-scan plane, we can more clearly implement and verify the quality of a semi-reverberant wave field from just two contact points. Given the constraint $\phi = 0$ and recomputing the ensemble average integral and autocorrelation along the plane orthogonal to the sensor axis z, we arrive at

$$B_{S_z S_z}(\Delta\varepsilon_x) = \frac{1}{2} j_0(k\Delta\varepsilon_x) - \frac{j_1(k\Delta\varepsilon_x)}{k\Delta\varepsilon_x}. \tag{4}$$

The autocorrelation is still a sum of spherical Bessel functions. However, the first term is scaled by half, which results in a narrowing of the central lobe of the Bessel function [Fig. 2(c)]. The autocorrelation function parallel to the sensor axis z remains the same as the fully reverberant case.

B. Experimental Setup

1. OCT System

The OCT data were acquired with a custom system, previously described in detail by Cannon *et al*. [37]: briefly, the system's laser was an optically k-clocked, phase-stable, 100 kHz VCSEL wavelength-swept laser (Thorlabs, SL131090) operating with a center wavelength of 1,310 nm. The collimated input beam had a diameter of 3.6 mm; combined with a 54 mm effective focal length objective scan lens (Thorlabs, LSM04), the system produced an e^{-2} diameter lateral resolution of 25 um. The beam was raster-scanned by galvanometers (Thorlabs, GVS002) through the scan lens with a field of view up to 14.1 mm. The galvanometers were aligned to avoid introducing a phase shift during scanning. The complex fringe was acquired with polarization diverse receivers (Advanced Fiber Resources). The incoming signal was digitized with a digitizer (AlazarTech, ATS 9373, 4 GS/s) with k-clocking. Displacements were computed from the Doppler phase differences [34] relative to the initial A-line at each location. We also applied surface wave correction [38] to compensate for sample surface motion and refractive index difference between the sample and air.

2. Fully Reverberant Materials and Methods

To validate our asynchronous shear wave field recovery technique, we built a homogeneous aqueous phantom with 1.5% (weight) agar and 0.5% (weight) intralipid. The phantom was imaged synchronously with 2 kHz piezoelectric excitation (Digi-key 445-181631-ND) and MB-mode scanning to obtain ground truth measurements of the shear wave field. The piezoelectric actuator was in contact with the phantom through eight independent 3D-printed prongs evenly spaced at a diameter of 20 mm. We acquired the synchronized B-scan with MB-mode scanning [Fig. 3(b)] by capturing 800 A-lines in a single location before moving onto the next. We did this at 1,024 locations across 5 mm. Since the repetition rate of the laser was 100 kHz and the shear waves were 2 kHz, each period of the shear wave field spanned exactly 50 A-lines. From the fully coherent data, we down-sampled to emulate the effect of raster-scanning by only keeping one A-line per global time step. We chose to emulate raster-scanning rather than measure it experimentally so we could use the synchronized data as ground truth for our demodulation pipeline and ensure both datasets were acquired at the same time. Then, we applied the demodulation pipeline to fully recover to the original coherent shear wave field. We repeated this experiment with experimental rather than emulated raster-scanning in Supplement 1. The entire signal processing pipeline for raster scanning is discussed in detail later.

3. Semi-reverberant Material and Methods

We also built a two-layer agar phantom with contrasting stiffness to demonstrate asynchronous semi-reverberant elastography in a heterogeneous sample. The lower stiff layer was composed of 1.5% (weight) agar, while the upper compliant layer was composed of 0.75% (weight) agar. The bottom layer was >10 mm thick, and

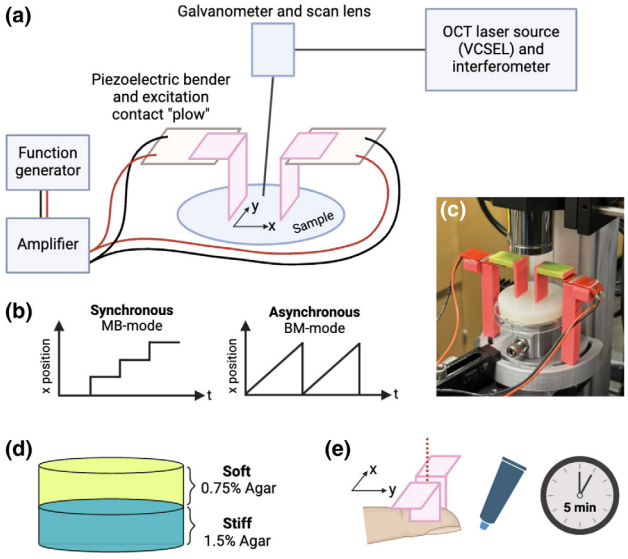

Fig. 3. We used a conventional OCT setup with a phase-stable laser (VCSEL) to acquire OCE images (a). The galvanometers can scan the OCT beam in either synchronous MB-mode or asynchronous BM-mode (b). The 3D-printed semi-reverberant plows are shown in (c) with a tissue-mimicking agar phantom. The two-layer agar phantom was composed of a lower stiff layer and upper compliant layer (d). For finger imaging, the thumb was placed between the plows with B-scans running across the finger pad (e). After acquiring data before hydration, lotion was applied. We waited 5 min before immediately acquiring a second dataset on the same finger (see Dataset 1, Ref. [39]).

the upper layer was 1.14 mm thick. Both layers had 0.5% (weight) intralipid so the OCT structural images would look identical despite each layer having different elastic properties. As depicted in Fig. 3(b), shear waves were excited in the sample by vertical plows that only generated waves in-plane with each B-scan. Shear waves were driven by a function generator through a high performance voltage amplifier (Micromechatronics Inc., MX200) and piezoelectric actuator (Digi-key 445-181631-ND). The data were acquired with the same raster-scanning, *k*-clocked, phase-stable, 100 kHz VCSEL wavelength-swept laser operating with a center wavelength of 1,310 nm. However, instead of synchronizing with the piezoelectric wave driver, the data were acquired conventionally by raster-scanning.

To acquire a full 4D volume, two consecutive B-scans of 1,792 A-lines each were first acquired along the x-axis consecutively. This is enough information to reconstruct the entire harmonic shear wave field at any point in time within that B-scan. Then, the beam was moved to the next out-of-plane y-location to acquire two more B-scans. This was repeated at 100 y-locations, resulting in a 4D volume with 1,792 samples along x and 100 samples along y, covering a 14×14 mm^2 field of view. This is essentially the same scanning paradigm used in OCT angiography. The number of A-lines was chosen to ensure Nyquist sampling across a 14 mm field of view, although this is not necessary if one does not plan on doing any post-processing such as non-uniform motion correction or optimum filtering. Given the laser sweep repetition rate and number of A-lines per B-scan, we chose 1,981 Hz for shear wave excitation to maximize displacement between B-scans (35.5 periods of the shear wave field).

Finally, we used asynchronous semi-reverberant elastography to image the ventral surface of a human finger *in vivo* before and after hydration. First, the skin was imaged prior to hydration with asynchronous semi-reverberant excitation. The plows were positioned on either side of the finger, running parallel to the length of the finger. B-scans were acquired across the finger, orthogonal to the plows. Then, the skin was lathered with thick lotion (Lubriderm, Advanced Therapy) for 5 min. After 5 min, the same region of skin was imaged [Fig. 3(e)]. Whereas existing methods would have taken up to 1 min to acquire these data, we were able to produce elastography measurements from only 3.58 s of imaging. This is a greater than 15-fold improvement in acquisition time, while also acquiring B-scans with 18× more A-line density. If the data were acquired with the same sparse A-line density used in prior reverberant studies, the overall improvement in acquisition time would have been over two orders of magnitude. Very importantly, similar to OCT angiography, only motion at the time scale of the repeated B-scans at each y location would affect our measurements; therefore, we have reduced the time scale of motion artifacts from 1 min to 36 ms, enabling the acquisition of data *in vivo*.

C. Signal Processing Pipeline

The following steps, illustrated in Fig. S1, describe in detail the signal processing pipeline used in MATLAB to measure shear modulus from an OCT volume. First, we regularized or flattened the tissue surface since the autocorrelation will be computed across the entire B-scan. Flattening allows us to separate the epidermis from the dermis more effectively, making our assumption of homogeneity more realistic. Dominant shear waves in strongly layered tissues such the skin are also likely to be either Rayleigh waves or Lamb waves, both of which travel horizontally along layers [40,41]. After flattening the tissue, the Doppler-OCT phase differences [34] were computed between A-lines at each location by multiplying one frame of the complex tomogram with the conjugate of another frame at a later time step. If the data were acquired with a polarization diverse receiver, the complex conjugates from each channel were summed before computing the phase. The phase difference is proportional to displacement by $S_z = (\lambda/4\pi n)\Delta\phi$, where S_z is the axial displacement, λ is the central wavelength of the laser, 1,300 nm, n is the refractive index of tissue that we approximate as 1.4, and $\Delta\phi$ is the Doppler phase difference. To reduce noise, we applied an anisotropic spatial Gaussian filter with a kernel size of 4 pixels along z and 1 pixel along x to the tomogram before computing the phase. We also applied surface wave correction [38] to compensate for sample surface motion and refractive index difference between the sample and air. See Code 1, Ref. [42] for practical implementation of these steps, as well as the rest of the signal processing pipeline steps.

With a phase-stable OCT system, there was negligible phase jitter or phase noise, which simplified processing. In a typical volume with two B-scans at 100 different y-locations, there were 200 total B-scans. After computing the Doppler phase difference, this was reduced to 100 displacement frames. We then performed 2D unweighted phase-unwrapping [43] along zx to get the unwrapped displacement field. Then, to demodulate the displacement field, we computed the 1D fast Fourier transform along x to get $\mathcal{F}_x\{S_z\}$. Three dominant peaks were observed: two peaks at the positive and negative carrier frequency in addition to one peak around zero for the DC component. We then downshifted the entire spectrum by the carrier frequency such that the desired signal was centered at zero. After downshifting, we

applied a rectangular window to the signal to retrieve the complex-valued displacement field with a reasonable spatial bandwidth. We define $\mathcal{D}\{\mathcal{F}_x\{S_z\};\ f,\ f_w\}$, where $\mathcal{D}$ represents the downshifting operator, f is the downshift amount (equal to the carrier frequency), and f_w is the width of the rectangular window. Given shear wave excitation frequency ω_0 and raster-scanning speed v_{scan}, $f = \omega_0 / v_{\text{scan}}$. Finally, we computed the inverse Fourier transform along x to recover the fully coherent complex-valued shear wave displacement field, $\mathcal{S} = \mathcal{F}_x^{-1}\{\mathcal{D}\{\mathcal{F}_x\{S_z\};\ f,\ f_w\}\}$.

From the complex-valued displacement field $\mathcal{S}$, we computed the autocorrelation along x. Note that prior work considered only the real part of the displacement, thus discarding half of the data. By considering the complex-valued field, we capture information from the entire harmonic period of the shear wave field from just one frame. The autocorrelation window spanned the entire length of x as well as a number of pixels along z for better averaging. We used 10 pixels in z, corresponding to 60 μm. Then, we found the best fit shear wave number k from the sum of square errors relative to Eq. (4). To dynamically adjust for tissue regions with different Bessel function widths, we found the second zero crossing and adjusted the fit length to only use the first two lobes. Since the autocorrelation spanned the entire width of a B-scan, we were left with a 1D set of k values at each y-location. From the shear wave number, we computed the shear wave speed c based on the shear wave frequency using $c = \omega_0 / k$. For a sample with constant density ρ, shear modulus G is directly related to shear wave speed by $c = \sqrt{G/\rho}$. Altogether, from an OCT volume with 1,000 pixels in depth, 1,792 A-lines per B-scan, and 200 B-scans, the resulting 2D shear wave number map consisted of 100 pixels in depth and 100 pixels across y.

3. RESULTS

A. Validation of Demodulation for Coherence Recovery

To demonstrate recovery of the coherent shear wave field while raster-scanning, we imaged an agar phantom with MB-mode synchronization for ground truth, then down-sampled the data to emulate scanning [Fig. 4]. For the fully synchronized data, we acquired 800 A-lines at 1,024 x-locations. Given the laser sweep repetition rate of 100 kHz and shear wave excitation of 2 kHz, each wave period consisted of 50 A-lines. We acquired 16 whole

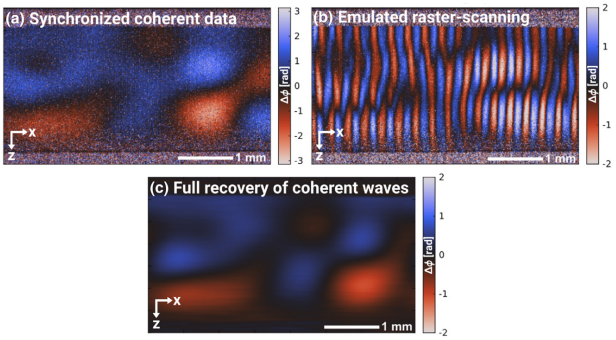

Fig. 4. Doppler phase differences from synchronous MB-mode imaging show a fully coherent shear wave field (a). By down-sampling (a) such that there is a delay between each A-line, we can emulate raster-scanning (b). The Doppler phase differences shown here (b) visually demonstrate the effect that multiplying by a higher frequency amplitude modulation term has on the displacement field. Finally, by computing the Fourier transform of (b), then downshifting, bandpass filtering, and inverse Fourier transforming, we recover the original fully coherent wave field (c).

periods of the shear wave field to ensure we had enough data in case the synchronization drifted. However, only 50 A-lines were strictly required. The raster-scanned data only required two A-lines per location after down-sampling, resulting in at least a 25-fold improvement in acquisition time (varying based on laser and shear wave frequency). Finally, we demodulated the amplitude modulation introduced by the raster-scanning time delay between A-lines to verify that the result was the same as the synchronized ground truth data. The results demonstrate successful recovery of the coherent wave field without need for slow synchronization [Fig. 4(c)]. The modulation effect also conveniently separates out our desired signal from low frequency noise by shifting the displacement field to the carrier frequency. Therefore, when we apply the bandpass filter to recover the displacement field, low frequency noise is also attenuated as part of the signal processing.

B. Elasticity Contrast in a Tissue-Mimicking Phantom

The foregoing analysis permits demodulation of the displacement field to recover spatial coherence. In this section, we demonstrate asynchronous semi-reverberant elastography in a tissue-mimicking phantom with elastic contrast [Fig. 5]. From the OCT intensity image, there is no major difference between the top and bottom layers besides their boundaries. The sample was excited with in-plane 1,981 Hz shear waves through two plows on either side of the field of view. Through demodulation, we recovered the spatially coherent displacement field along x, from which we also computed the autocorrelation. By applying the rest of our signal processing pipeline, we can measure the shear wave number k as well as the shear modulus G. Note that the data were collected entirely with conventional raster-scanning, and we were able to use the methods described herein to successfully recover the coherent displacement field [Fig. 5(b)]. This enabled us to use the in-plane semi-reverberant Bessel function sums that we derived [see Eq. (4)] to fit shear wave number. As expected, since shear wavelength is larger in stiffer tissue, the central lobe of the autocorrelation in the bottom layer was wider [Fig. 5(d)]. Since the phantom was homogeneous along x, and we computed the autocorrelation along the entire x dimension, collapsing each xz-plane of data to a single dimension of k values allows us to present elastography results along the yz-plane.

For the purpose of demonstration, we also present data from out-of-plane shear wave excitation in Supplement 1. While we were able to successfully recover the coherent shear wave displacement field, elastography measurements do not accurately reveal a compliant upper layer and stiff lower layer [Fig. S1]. This is due to the distortion of out-plane waves, highlighting the critical and necessary development of in-plane shear wave excitation for raster-scanned, asynchronous, semi-reverberant elastography.

C. Elasticity before and after Hydration *in Vivo*

Asynchronous semi-reverberant elastography drastically reduces acquisition time and enables elasticity imaging *in vivo*. Here, to the best of our knowledge, we present the first reverberant elastography results acquired with a conventional, raster-scanning OCT system without synchronization or complex, custom hardware by reducing acquisition time from minutes to seconds [Fig. 6]. The data were collected on skin from the ventral surface of a human finger before and after hydration with lotion. Our experimental results *in vivo* demonstrate the feasibility of our technique for diagnosing

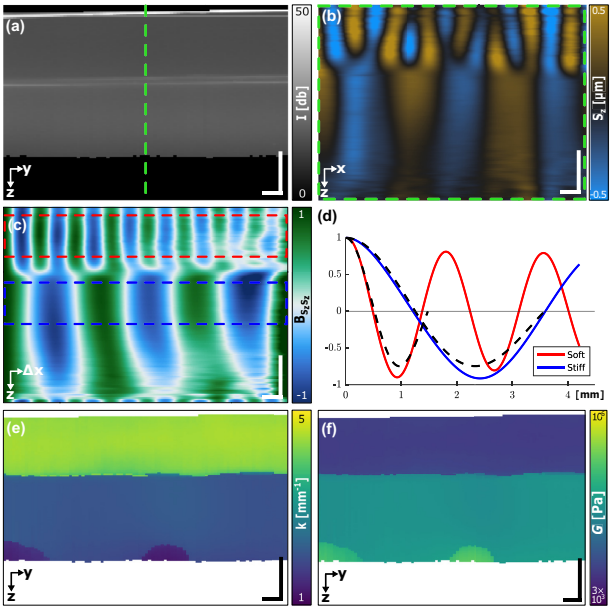

Fig. 5. OCT structural image of the x-averaged, yz-plane view of the phantom, where the colorbar indicates the signal-to-noise ratio (SNR) in logarithmic scale (a). One frame of the coherent displacement field at the location marked by the green dashed line in (a) is shown in (b). From the coherent field, we compute the normalized autocorrelation along x for each depth. The one-sided Bessel function at each depth is displayed to appreciate the boundary between soft and stiff (c). The average autocorrelation within the red and blue windows for the compliant and stiff regions, respectively, are shown in (d), as well as the Bessel function that was fit to them (black dashed line). We typically use up to the second zero crossing to fit Bessel functions. As expected, smaller wavelength waves in the compliant region have a narrower central lobe. We can measure this quantitatively by fitting k to each Bessel function, thus arriving at (e), which shows a clear demarcation between layers. We can also compute the quantitative shear modulus (f). Scale bars are 1 mm.

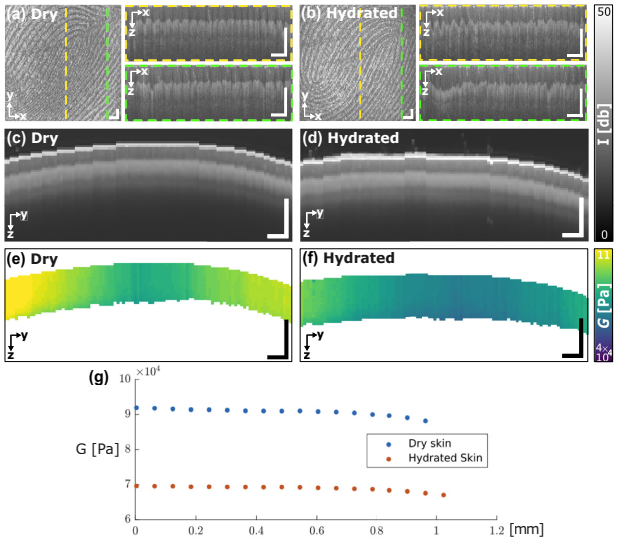

Fig. 6. The fields of view before (a) and after (b) hydration (alongside two B-scan cross sections each) demonstrate there is no remarkable difference between OCT structural images of the finger before or after hydration (a)–(d), where the colorbar indicates the signal-to-noise ratio (SNR) in logarithmic scale. However, the measured shear moduli before (e) and after (f) hydration clearly demonstrate a difference in elasticity. Results are displayed along the yz-plane due to fitting the Bessel function sum along x. The depth dependent shear modulus averaged across each horizontal layer also clearly demonstrates expected softening of the skin upon hydration (g). Scale bars are 1 mm.

and/or monitoring pathologies in patients correlated with skin elasticity, such as skin cancer lesions and systemic sclerosis [31–33].

OCT intensity images of the x-averaged yz-plane show there is no difference in the structure of the tissue before or after hydration. We can also see the epidermis, dermis, and hypodermis layers. For our processing, we flattened the tissue to enable averaging across the entire x direction without significant mixing of different regions of tissue. The tissue was not flattened along the y-direction, as seen in Figs. 6(a) and 6(b). We acquired volumes with 200 B-scans, each with 1,792 A-lines, resulting in a total acquisition time of 3.58 s. During acquisition, we applied 1,981 Hz in-plane shear wave excitation with plows. The data were raster-scanned, with two consecutive B-scans at each of 100 y-locations. The 14 × 14 mm field of view *en face* OCT intensity image of the surface of the finger is shown in Fig. 6(e). From each 3D volume we measured a 2D map of shear wave numbers k. Shear wave numbers are related to shear modulus by tissue density, so assuming a constant tissue density, we can also measure the quantitative shear modulus. Finally, we computed the depth dependent shear modulus for dry versus hydrated skin. This is the shear modulus at each depth, averaged across the entire layer. As expected, dry skin has a higher shear modulus compared to hydrated skin [44,45]. Compared to other studies of elastography in skin, these measurements of shear modulus are within a reasonable range. For example, Feng *et al.* [46,47] measure the shear modulus around 10 kPa for skin in the low kHz frequency range and in the dermis layer. One difference is that these results do not demonstrate the same contrast in the epidermis, and this is likely due to the dispersion of leaky Rayleigh surface waves. At 2 kHz, the shear wave is primarily dominating in the dermis layer of the tissue. While it is certainly detrimental to resolution to average over the entire lateral field of view, this is up to par with current state-of-the-art methods [26,46], while taking less time to acquire.

4. DISCUSSION

Reverberant elastography is capable of producing remarkable measures of elasticity. By leveraging a diffuse and dynamic shear wave field, it is also relatively robust to motion, making it a promising candidate for translation *in vivo*. Despite these potential benefits, implementations of existing reverberant methods (as well as wave-based OCE methods in general) are still fundamentally limited by their need to synchronize shear wave excitation with MB-mode imaging. Since acquisition time is long with MB-mode scanning, existing methods tend to drastically under sample in the horizontal dimension, leaving us further unable to correct the signal for motion artifacts or otherwise with speckle-based methods. (While they may not sample the OCT beam itself finely enough, they do, however, sample the shear wave field itself with enough resolution to measure shear wavelength.) Instead, the patient or sample must remain completely still for up to minutes at a time, which is impractical for most clinical applications *in vivo* such as in the eye, and even more so for OCT probes or catheters. Notably, these limitations are not due to the fundamental principles of reverberant elastography. Rather, they are a practical limitation unique to raster-scanned systems such as OCT and their slow frame rates relative to typical shear wave speeds.

In this work, we addressed these limitations with three key advances. First, leveraging displacement rather than velocity removed temporal sampling requirements, thus enabling conventional raster-scanning. Second, the time delay between A-lines that arise from raster-scanning can be successfully demodulated to recover the coherent shear wave field without any need for arduous synchronization efforts. Finally, since demodulation only exists along the x-axis, we presented a novel shear wave excitation scheme that only produces waves traveling in-plane along B-scans. All together, these achievements enabled reverberant elastography *in vivo* by drastically reducing acquisition time by *two orders of magnitude* for the same lateral sampling parameters typically used in previous work. For laterally Nyquist-sampled data, total imaging speed is still faster by an order of magnitude, while enabling a multitude of advanced signal processing techniques, such as non-linear speckle-based motion correction or optimum filtering. Beyond reverberant elastography, this work also has implications for the field of wave-based OCE as a whole. Prior work in single wavefront dynamic OCE, such as that by Feng *et al*. [46], has also leveraged demodulation to image shear wave speeds previously inaccessible by conventional techniques. However, they use frequency demodulation (rather than amplitude modulation) only along the A-line axis to access ultra-high shear wave frequencies up to MHz, and synchronized scanning is still required. The scan patterns used in this work are already compatible with existing scan patterns used in OCT angiography, which may acquire up to 4 B-scans per location [48], further reducing the barrier to translation. Crawling wave OCE methods [49,50] use similar but slightly different frequency shakers to generate a slow-moving crawling wave that may be imaged by conventional raster-scanning rates. The semi-reverberant field is distinct from the crawling wave because both piezoelectric actuators are driven at the same frequency, yet we do not observe a standing wave pattern. We also do not rely on slowing down the apparent speed of shear waves. To this point, we could just excite only on one side of the B-scan, although a semi-reverberant field is more easily achieved with multiple excitation sources. Furthermore, the distances between semi-reverberant excitation sources and their respective coupling efficiencies are more flexible, leading to fewer restrictions compared those required to generate crawling waves. The semi-reverberant field may therefore also be more robust in heterogeneous media where the amplitude of each wave reaching the imaging site may be different due to attenuation. Crawling wave methods also appear to utilize a point source, rather than an entire line source such as the plows, thus generating spherical waves rather than plane waves within the OCT field of view.

While this work has opened up the door for more practical clinical translation of reverberant elastography, limitations remain. For one, direct contact with tissue to generate shear waves is undesirable. Even if image acquisition rates are reduced from minutes to seconds or milliseconds, it is still best not to directly contact sensitive tissue such as the eye. It is furthermore impractical to use direct contact in a probe or catheter due to the intrinsic motion of the patient and the operator. Therefore, methods such as acoustic radiation force or other non-contact methods are essential. Additionally, our ability to only achieve coherence along the x-axis means that the tissue must be relatively homogeneous along x. Reverberant elastography will also always be limited by the autocorrelation window size, which is limited by the shear wavelength. This is because the window must be large enough to capture most of the central lobe of the Bessel function sum: the larger the shear wavelength is, the larger size a window must be. One method to reduce shear wavelength is to increase shear wave frequency; however, higher frequency waves attenuate more rapidly, making it harder to produce a diffuse wave field.

Another limitation of all wave-based methods arises when we consider the waveguide-like nature of biological tissues. This effect is especially true for understanding shear wave behavior in heterogeneous or strongly layered tissues. Given different shear wave frequencies and orientations, as well as varying tissue properties and geometry, shear waves are likely to have different distinct guided modes, which will impact reverberant calculations. With our technique, by focusing on in-plane shear waves, we are at least able to reduce the need to rely on a diffuse regime in all directions. The leaky wave effect also implies that shear waves are not necessarily bounded by changes in biomechanical properties. Instead, to maintain continuity, softer tissue may sometimes host shear waves that are larger than they would be otherwise due to sharing a boundary with much stiffer tissue. Since evanescent waves decay at a length comparable to the wavelength, this is generally negligible in the optical regime; however, since shear wavelength in tissue is on the order of mm, the evanescent wave effect can strongly distort measured layer boundaries in depth. Depending on the relative stiffness and thickness of each part of the tissue, the magnitude of the effect changes. Therefore, for each potential clinical application, it is critical to understand the underlying tissue architecture and expected range of shear wave speeds in order to design the most effective imaging scheme.

5. CONCLUSION

In this work, we demonstrated asynchronous semi-reverberant elastography in human skin *in vivo*. Whereas previous methods were slow and sensitive to motion, this new method is relatively robust against motion, which enabled us to produce images of elasticity *in vivo*. Using the displacement rather than the velocity allowed us to overcome temporal coherence sampling requirements. Furthermore, by accounting for the time delay between A-lines that is inherent to raster-scanning, we showed that we can model scanning as a form of amplitude modulation. Demodulation of the raster-scanning term therefore enables direct recovery of the coherent and harmonic shear wave field. Since this method is only effective along the B-scan axis, we have also revised the reverberant elastography model to only include in-plane waves. All together, these advancements each played a critical role in enabling the measurement of 2D elasticity contrast in a layered tissue-mimicking phantom, as well as in human skin before and after hydration. To the best of our knowledge, these are the first reverberant elastography results acquired with a conventional frame-rate, raster-scanning OCT system without the need for synchronization or complex, custom hardware, hence reducing acquisition time from minutes to seconds and opening the door for practical clinical translation.

Funding. National Science Foundation Graduate Research Fellowship Program; National Institutes of Health (K25EB024595, P41EB015903, R01EB033306).

Disclosures. The authors declare no conflicts of interest.

Data availability. Data may be obtained from the authors upon reasonable request. Sample processing scripts and test data are available at Code 1, Ref. [42] and Dataset 1, Ref. [39].

Supplemental document. See Supplement 1 for supporting content.

REFERENCES

1. D. Huang, E. A. Swanson, C. P. Lin, *et al.*, "Optical coherence tomography," Science **254**, 1178–1181 (1991).
2. I. Laíns, J. C. Wang, Y. Cui, *et al.*, "Retinal applications of swept source optical coherence tomography (OCT) and optical coherence tomography angiography (OCTA)," Prog. Retinal Eye Res. **84**, 100951 (2021).
3. M. A. Kirby, I. Pelivanov, S. Song, *et al.*, "Optical coherence elastography in ophthalmology," J. Biomed. Opt. **22**, 121720 (2017).
4. B. E. Bouma, J. F. De Boer, D. Huang, *et al.*, "Optical coherence tomography," Nat. Rev. Methods Primers **2**, 79 (2022).
5. M. Singh, F. Zvietcovich, and K. V. Larin, "Introduction to optical coherence elastography: tutorial," J. Opt. Soc. Am. A **39**, 418–430 (2022).
6. R. Ambekar, K. C. Toussaint, Jr., and A. W. Johnson, "The effect of keratoconus on the structural, mechanical, and optical properties of the cornea," J. Mech. Behav. Biomed. Mater. **4**, 223–236 (2011).
7. D. P. Piñero, J. L. Alio, R. I. Barraquer, *et al.*, "Corneal biomechanics, refraction, and corneal aberrometry in keratoconus: an integrated study," Invest. Ophthalmol. Vis. Sci. **51**, 1948 (2010).
8. J. C. Downs, M. D. Roberts, and C. F. Burgoyne, "Mechanical environment of the optic nerve head in Glaucoma," Optometry Vis. Sci. **85**, E425–E435 (2008).
9. C. F. Guimarães, L. Gasperini, A. P. Marques, *et al.*, "The stiffness of living tissues and its implications for tissue engineering," Nat. Rev. Mater. **5**, 351–370 (2020).
10. S. Nandy, R. A. Raphaely, A. Muniappan, *et al.*, "Diagnostic accuracy of endobronchial optical coherence tomography for the microscopic diagnosis of usual interstitial pneumonia," Am. J. Resp. Crit. Care Med. **204**, 1164–1179 (2021).
11. J. T. Pruijssen, C. L. de Korte, I. Voss, *et al.*, "Vascular shear wave elastography in atherosclerotic arteries: a systematic review," Ultrasound Med. Biol. **46**, 2145–2163 (2020).
12. P. Doradla, K. Otsuka, A. Nadkarni, *et al.*, "Biomechanical stress profiling of coronary atherosclerosis: identifying a multifactorial metric to evaluate plaque rupture risk," JACC: Cardiovasc. Imaging **13**, 804–816 (2020).
13. J. M. Schmitt, "OCT elastography: imaging microscopic deformation and strain of tissue," Opt. Express **3**, 199 (1998).
14. V. Y. Zaitsev, A. L. Matveyev, L. A. Matveev, *et al.*, "Strain and elasticity imaging in compression optical coherence elastography: the two-decade perspective and recent advances," J. Biophoton. **14**, e202000257 (2021).
15. A. Nair, M. Singh, S. R. Aglyamov, *et al.*, "Heartbeat OCE: corneal biomechanical response to simulated heartbeat pulsation measured by optical coherence elastography," J. Biomed. Opt. **25**, 055001 (2020).
16. J. Brum, N. Benech, T. Gallot, *et al.*, "Shear wave elastography based on noise correlation and time reversal," Front. Phys. **9**, 617445 (2021).
17. F. Zvietcovich, J. P. Rolland, J. Yao, *et al.*, "Comparative study of shear wave-based elastography techniques in optical coherence tomography," J. Biomed. Opt **22**, 035010 (2017).
18. F. Zvietcovich and K. V. Larin, "Wave-based optical coherence elastography: the 10-year perspective," Prog. Biomed. Eng. **4**, 012007 (2022).
19. M. A. Kirby, J. J. Pitre, H.-C. Liou, *et al.*, "Delineating corneal elastic anisotropy in a porcine model using noncontact OCT elastography and ex vivo mechanical tests," Ophthalmol. Sci. **1**, 100058 (2021).
20. M. A. Kirby, P. Tang, H.-C. Liou, *et al.*, "Probing elastic anisotropy of human skin in vivo with light using non-contact acoustic micro-tapping OCE and polarization sensitive OCT," Sci. Rep. **12**, 3963 (2022).
21. M. A. Kirby, I. Pelivanov, G. Regnault, *et al.*, "Acoustic micro-tapping optical coherence elastography to quantify corneal collagen cross-linking," Ophthalmol. Sci. **3**, 100257 (2023).
22. A. Ramier, A. M. Eltony, Y. Chen, *et al.*, "In vivo measurement of shear modulus of the human cornea using optical coherence elastography," Sci. Rep. **10**, 17366 (2020).
23. K. J. Parker, J. Ormachea, F. Zvietcovich, *et al.*, "Reverberant shear wave fields and estimation of tissue properties," Phys. Med. Biol. **62**, 1046–1061 (2017).
24. V. Emiliani, F. Intonti, M. Cazayous, *et al.*, "Near-field short range correlation in optical waves transmitted through random media," Phys. Rev. Lett. **90**, 250801 (2003).
25. A. Apostol and A. Dogariu, "Spatial correlations in the near field of random media," Phys. Rev. Lett. **91**, 093901 (2003).
26. F. Zvietcovich, P. Pongchalee, P. Meemon, *et al.*, "Reverberant 3D optical coherence elastography maps the elasticity of individual corneal layers," Nat. Commun. **10**, 4895 (2019).
27. G. R. Ge, W. Song, M. Nedergaard, *et al.*, "Theory of sleep/wake cycles affecting brain elastography," Phys. Med. Biol. **67**, 225013 (2022).
28. M. Singh, F. Zvietcovich, C. Zevallos-Delgado, *et al.*, "Whole embryo biomechanics with reverberant optical coherence elastography," Optica **11**, 686–692 (2024).
29. M. Singh, A. W. Schill, A. Nair, *et al.*, "Ultra-fast dynamic line-field optical coherence elastography," Opt. Lett. **46**, 4742–4744 (2021).
30. S. Burhan, N. Detrez, K. Rewerts, *et al.*, "Phase unwrapping for MHz optical coherence elastography and application to brain tumor tissue," Biomed. Opt. Express **15**, 1038 (2024).
31. P. Sobolewski, M. Maślińska, J. Zakrzewski, *et al.*, "Applicability of shear wave elastography for the evaluation of skin strain in systemic sclerosis," Rheumatol. Int. **40**, 737–745 (2020).
32. B. Dasgeb, M. A. Morris, D. Mehregan, *et al.*, "Quantified ultrasound elastography in the assessment of cutaneous carcinoma," Br. J. Radiol. **88**, 20150344 (2015).
33. F. H. Silver, N. Kelkar, T. Deshmukh, *et al.*, "Characterization of the biomechanical properties of skin using vibrational optical coherence tomography: do changes in the biomechanical properties of skin stroma reflect structural changes in the extracellular matrix of cancerous lesions?" Biomolecules **11**, 1712 (2021).
34. R. A. Leitgeb, R. M. Werkmeister, C. Blatter, *et al.*, "Doppler optical coherence tomography," Prog. Retinal Eye Res. **41**, 26–43 (2014).
35. G. Flores, J. Ormachea, S. E. Romero, *et al.*, "Experimental study to evaluate the generation of reverberant shear wave fields (R-SWF) in homogenous media," in *IEEE International Ultrasonics Symposium (IUS)* (IEEE, 2020), pp. 1–4.
36. I. E. Kabir, D. A. Caban-Rivera, J. Ormachea, *et al.*, "Reverberant magnetic resonance elastographic imaging using a single mechanical driver," Phys. Med. Biol. **68**, 055015 (2023).
37. T. M. Cannon, B. E. Bouma, and N. Uribe-Patarroyo, "Layer-based, depth-resolved computation of attenuation coefficients and backscattering fractions in tissue using optical coherence tomography," Biomed. Opt. Express **12**, 5037 (2021).
38. S. Song, Z. Huang, and R. K. Wang, "Tracking mechanical wave propagation within tissue using phase-sensitive optical coherence tomography: motion artifact and its compensation," J. Biomed. Opt. **18**, 121505 (2013).
39. G. Schmidt and N. Uribe-Patarroyo, "tom.mat dataset," figshare, 2024, https://doi.org/10.6084/m9.figshare.26530843.v1.
40. K. Worden, "Rayleigh and lamb waves—basic principles," Strain **37**, 167–172 (2001).
41. Z. Han, J. Li, M. Singh, *et al.*, "Optical coherence elastography assessment of corneal viscoelasticity with a modified Rayleigh-Lamb wave model," J. Mech. Behav. Biomed. Mater. **66**, 87–94 (2017).
42. G. Schmidt and N. Uribe-Patarroyo, "Asynchronous, semi-reverberant elastography," code, 2024, https://github.com/gingerschmidt/AsyncSemiReverb.
43. D. C. Ghiglia and L. A. Romero, "Robust two-dimensional weighted and unweighted phase unwrapping that uses fast transforms and iterative methods," J. Opt. Soc. Am. A **11**, 107–117 (1994).
44. M. Qassem and P. Kyriacou, "Review of modern techniques for the assessment of skin hydration," Cosmetics **6**, 19 (2019).
45. S. Verdier-Sévrain and F. Bonté, "Skin hydration: a review on its molecular mechanisms," J. Cosmet. Dermatol. **6**, 75–82 (2007).
46. X. Feng, G.-Y. Li, and S.-H. Yun, "Ultra-wideband optical coherence elastography from acoustic to ultrasonic frequencies," Nat. Commun. **14**, 4949 (2023).
47. X. Feng, G.-Y. Li, A. Ramier, *et al.*, "In vivo stiffness measurement of epidermis, dermis, and hypodermis using broadband Rayleigh-wave optical coherence elastography," Acta Biomaterialia **146**, 295–305 (2022).
48. A. Javed, A. Khanna, E. Palmer, *et al.*, "Optical coherence tomography angiography: a review of the current literature," J. Int. Med. Res. **51**, 03000605231187933 (2023).

49. A. Partin, Z. Hah, C. T. Barry, *et al.*, "Elasticity estimates from images of crawling waves generated by miniature surface sources," Ultrasound Med. Biol. **40**, 685–694 (2014).

50. C. T. Barry, Z. Hah, A. Partin, *et al.*, "Mouse liver dispersion for the diagnosis of early-stage fatty liver disease: a 70-sample study," Ultrasound Med. Biol. **40**, 704–713 (2014).